

Supplementary information for
Real-Time *In Situ* Observations Reveal a Double Role for Ascorbic Acid in the Anisotropic Growth of Silver on Gold

Kinanti Aliyah¹, Jieli Lyu¹, Claire Goldmann¹, Thomas Bizien², Cyrille Hamon^{1*}, Damien Alloeyau^{3*}, and Doru Constantin^{1*}

¹Université Paris-Saclay, CNRS, Laboratoire de Physique des Solides, 91405 Orsay, France.

²SWING beamline, SOLEIL Synchrotron, Gif-sur-Yvette, France.

³Laboratoire Matériaux et Phénomènes Quantiques, Université de Paris - CNRS, F-75013, Paris, France.

Table of contents

| | |
|---|----|
| Materials and methods | 2 |
| Nanoparticle Preparation | 2 |
| Characterization | 4 |
| Liquid-cell STEM | 4 |
| UV-Vis-NIR Spectroscopy..... | 4 |
| SAXS experiments..... | 5 |
| Derivation of the equation for the length evolution in time | 6 |
| Supplementary Figures..... | 8 |
| Supplementary Movies | 23 |
| References..... | 24 |

Materials and methods

Nanoparticle Preparation

Materials – All the starting materials were obtained from commercial suppliers and used without further purification: hexadecyltrimethylammonium bromide (CTAB, $\geq 99\%$), hexadecyltrimethylammonium chloride (CTAC, 25 wt % in H_2O , 90%), hydrogen tetrachloroaurate trihydrate ($\text{HAuCl}_4 \cdot 3\text{H}_2\text{O}$, $\geq 99.9\%$), silver nitrate (AgNO_3 , $\geq 99.0\%$), L-ascorbic acid (AA, $\geq 99\%$), sodium borohydride (NaBH_4 , 99%), trisodium citrate ($\geq 99.0\%$). Water purified by reverse osmosis with a resistivity ($>15 \text{ M}\Omega \cdot \text{cm}$) was used for the synthesis of the nanocrystals which were purified with Milli-Q water (resistivity $18.2 \text{ M}\Omega \cdot \text{cm}$) prior to LCTEM experiments.

Synthesis of Gold Pentatwinned Seeds – Synthesis of gold pentatwinned seeds was adapted from the literature.¹⁻² In a 100 mL Erlenmeyer flask, 37 mL of a 60.6 mM CTAC solution was constituted in which 400 μL of 25 mM HAuCl_4 and 4 mL of 50 mM sodium citrate were added in sequence. The solution was kept in a water bath with at 30°C for 10 minutes under gentle stirring. Then, 2.4 mL of a 10 mM NaBH_4 solution was injected under vigorous stirring. A reddish solution was obtained after aging the samples during 5 days at 40°C . The seed solution can be stored for at least one month at 25°C .

Synthesis of Gold Bipyramids – In a 250 mL Erlenmeyer flask, growth solution was prepared by the successive addition of 100 mL of 0.1 M CTAB, 1 mL of 10 mM AgNO_3 , 2 mL of 25 mM HAuCl_4 and 2 mL of 1 M HCl . Then, 800 μL of a 100 mM AA solution was added under vigorous stirring, followed by the addition of 900 μL of seed solution. The mixture was left undisturbed at 30°C for at least 4 h. After synthesis, particles were purified by at least two cycles of centrifugation and pellet redispersion in $[\text{CTAC}] = 10 \text{ mM}$ in order to obtain a dispersion of 0.25 mM (in Au^0) and 10 mM CTAC. The NPs dispersion can be stored for months in ambient conditions.

Synthesis of Au@Ag rods – Silver overgrowth on gold bipyramid seeds was performed according to recently published protocols.³⁻⁵ The purified NPs dispersion was supplemented with a 10 mM AgNO₃ solution and a 40 mM AA solution in equal volumes, to fix the molar ratio of between the Ag precursor and AA to 4. To vary the length of the Au@Ag rods, the silver to gold molar ratio was adjusted as described in Table 1. After mixing, the reaction vials were kept at 60°C for 3h to yield Au@Ag rods.

Table 1. Details on volumes of reactants used for the preparation of Au@Ag rods. The column highlighted in gray corresponds to the conditions used in the preparation of the particles in Figure 2 and 3 of the main text. While growth kinetics could be investigated by our *in situ* approach, the final length of the particles in the case of Ag/Au ratio of 5, 10, 15, could not be retrieved because the LSPR shifted outside the experimental accessible range.

| Ag/Au | 0 | 0.5 | 1 | 3 |
|------------------------------|----------|------------|----------|----------|
| 0.25 mM Au sol (μL) | 500 | 500 | 500 | 500 |
| 10 mM AgNO ₃ (μL) | 0 | 6.2 | 12.5 | 37.5 |
| 40 mM AA (μL) | 0 | 6.2 | 12.5 | 37.5 |
| <i>W</i> (nm) | 21.4 | 23.0 | 23.3 | 24.0 |
| <i>L</i> (nm) | 71.7 | 71.7 | 71.7 | 192.8 |

| Ag/Au | 5 | 10 | 15 |
|-------------------------------|----------|-----------|-----------|
| 0.25 mM Au sol (μL) | 500 | 500 | 500 |
| 100 mM AgNO ₃ (μL) | 6.2 | 12.5 | 18.7 |
| 400 mM AA (μL) | 6.2 | 12.5 | 18.7 |
| <i>W</i> (nm) | 24.7 | 25.2 | 25.3 |
| <i>L</i> (nm) | >202 | >202 | >202 |

Characterization

Liquid-cell STEM – Liquid STEM imaging was performed on a JEOL ARM 200F microscope operating at 200 kV, using a liquid-cell TEM holder (Poseidon select, Protochips inc.). A colloidal suspension of gold bipyramidal seeds (with a gold concentration of 0.25 mM) dispersed in a CTAC aqueous solution (10 mM) was encapsulated in the liquid-cell by using the conventional loading process.⁶⁻⁷ When ascorbic acid was present in the reaction media, its concentration was 2.25 mM. The Au spacers of the liquid cell were 150 nm thick and the experiments were performed in the corners of the observation window, where the liquid thickness is minimum. The liquid cell was used in static mode. Growth experiments were performed before and after the formation of a hydrogen bubble in the liquid cell that improves the signal to noise ratio of images. We did not notice any difference in the growth processes of Au@Ag nanoparticles with or without the hydrogen bubble. STEM HAADF imaging was performed with a pixel dwell time of 5 μ s and probe current ranging from $7.7 \cdot 10^7$ to $4.7 \cdot 10^8$ electron/s. The electron dose rate of each growth experiments was calculated in $\text{electron} \cdot \text{s}^{-1} \cdot \text{nm}^{-2}$ by dividing the probe current by the irradiated area (i.e. the image area in STEM mode). STEM diffraction was performed after the formation of the hydrogen bubble with a probe current of 10^8 electron/s.⁸

UV-Vis-NIR Spectroscopy – Measurements were carried out with a Cary 5000 UV-Vis-NIR Spectrometer. *In situ* monitoring of the Au@Ag rods synthesis was performed by loading the reaction mixture in a sealed optical capillary (0.3 mm thick) and mounted in a Linkam stage. The temperature was varied between 40 and 80°C in separated experiments.

BEM modelling - Simulated extinction spectra were calculated by the boundary element method (BEM), using the MNPBEM toolbox developed in the MATLAB environment.⁹ The gold bipyramidal seed is described as a gold bicone with 73.3 nm in length and 25.9 nm in base-width, terminated with two spherical caps. The silver shell is described as a spherocylinder of 28.5 nm width and varying length. For simulations, each particles were modeled with a triangular mesh consisting of more than 1000 faces. Simulations were performed to solve the full Maxwell's equations (including retardation effects). The dielectric properties of gold and silver were taken from P. B. Johnson and R. W. Christy.¹⁰ We first simulated rods of varying length in order to determine a relation between LSPR position and the rods aspect ratio (L/W). With W precisely determined from SAXS, we retrieve an estimation of the evolution of the length over time as shown in Figure 2d. The experimental peak width is larger than the simulated one due to the length polydispersity; we can thus estimate this parameter, as discussed below.

SAXS experiments – The SAXS data was collected at the SWING beamline of the SOLEIL synchrotron (Saint-Aubin, France), at a beam energy of 16 keV and sample-to-detector distances 6.52 m, with an exposure time of 2 s and a gap time of 2 s for each image. The samples (with a volume of 60 μ L) were contained in cylindrical glass capillaries (Mark-Rörchen, Germany) of calibrated diameter, placed in a motorized and temperature-controlled holder. The scattered signal was recorded by an Eiger 4M detector (Dectris Ltd., Switzerland) with pixel size 75 μ m. Preliminary data treatment (angular averaging and normalization) was done using the software Foxtrot developed at the beamline and yielded the intensity as a function of the scattering vector $I(q)$ in absolute units. Background subtraction was done by subtraction data with capillaries of same diameter filled with water. Subsequent data fitting was done in Igor Pro using the sum of two models available in the NCNR SANS package:¹¹ the form factor model for a cylinder population

with polydisperse radius, describing the Au/Ag nanorods, and a one-level Beaucage model, accounting for other particles with ill-defined geometry: seeds with other morphologies leading to other Au/Ag core-shell nanostructures and possibly silver nanoparticles growing alongside Au@Ag nanorods. The explicit equation for the one-level Beaucage model is given below:

$$I_B(q) = Ge^{-\frac{q^2 R_g^2}{3}} + B \frac{[\text{erf}(qR_g/\sqrt{6})]^{12}}{q^4}$$

A fit example is provided in Supplementary Figure 5a, while Figures 5b and 5c show respectively the width evolution over time and the final width for all Ag/Au ratios.

Assuming that the entire $I_B(q)$ contribution is due to seedless silver nanoparticles, we can estimate the proportion of the latter among the reaction products at about 20 %, based on the total integrated intensity (the invariant).

Derivation of the equation for the length evolution in time

We detail the reasoning behind Equation (1) in the main text for the time dependence of the rod length $L(t)$. A similar derivation has already been presented in the literature.¹² The parameter of interest is the time-dependent concentration $\phi(t)$ of Ag atoms that is contained in the metal nanoparticles. Since we only consider one-dimensional growth, the average length $L(t) \equiv \langle L \rangle(t) \sim \phi(t)/N_s$, where N_s is the total number of seeds (gold bipyramids) per unit volume in solution.

Depending on the exact process, not all seeds may be active at all times, so we denote by $N(t)$ the concentration of growing particles. The differential equation for $\phi(t)$ is then (up to inessential prefactors):

$$d\phi = N(t)Sk[(1 - \phi(t)) - \phi_c] dt$$

It simply states that the $N(t)$ particles grow via a flux of Ag atoms arriving onto their active surface of size S (roughly, twice the “tip area”) in accordance to Fick’s law: the flux is proportional to the difference between the concentration of ionic Ag ($1-\phi$) and a critical value ϕ_c below which the growth stops.

If all seeds are active throughout the process, $N(t) = N_s$ and the equation yields a simple exponential dependence: $\phi(t) = (1 - \phi_c) - \exp(-\alpha t)$. If, on the other hand, the seeds become gradually activated via (for instance) a linear law $N(t) = \Delta \cdot t$, with the rate Δ low enough so that $N(t)$ does not exceed N_s during the growth process, the concentration behaves like a compressed exponential with compression exponent $k = 2$:

$$\phi(t) = (1 - \phi_c) - \exp[-(\beta t)^2],$$

in agreement with the classical version of the Avrami equation, where this exponent is the sum of two terms, one representing growth dimensionality and the other the “activation rate”.¹³ In our case, each of these terms equals one. Here, the computed $L(t)$ is the mean of the length distribution. The gradual activation of the seeds would imply that the width of this distribution should increase over time.

To check this conclusion we analyzed the extinction peaks in Figure S4 and extracted the particle length polydispersity $\sigma_L(t)$ using the same linear relation as for $L(t)$ (red line fit in Figure S6) from the peak width $\Delta\lambda(t)$, after subtracting the width of the BEM models with the same peak position (solid lines in Figure S16a). The values for $L(t)$ and $\sigma_L(t)$ are shown in Figure S16b as symbols and error bars, respectively.

The relative polydispersity $\sigma_L/L(t)$ increases from 2 % to 13 % from the beginning of the lengthening process (labeled as “red shift” in Figure S16b) to time $t = 3000$ s.

Supplementary Figures

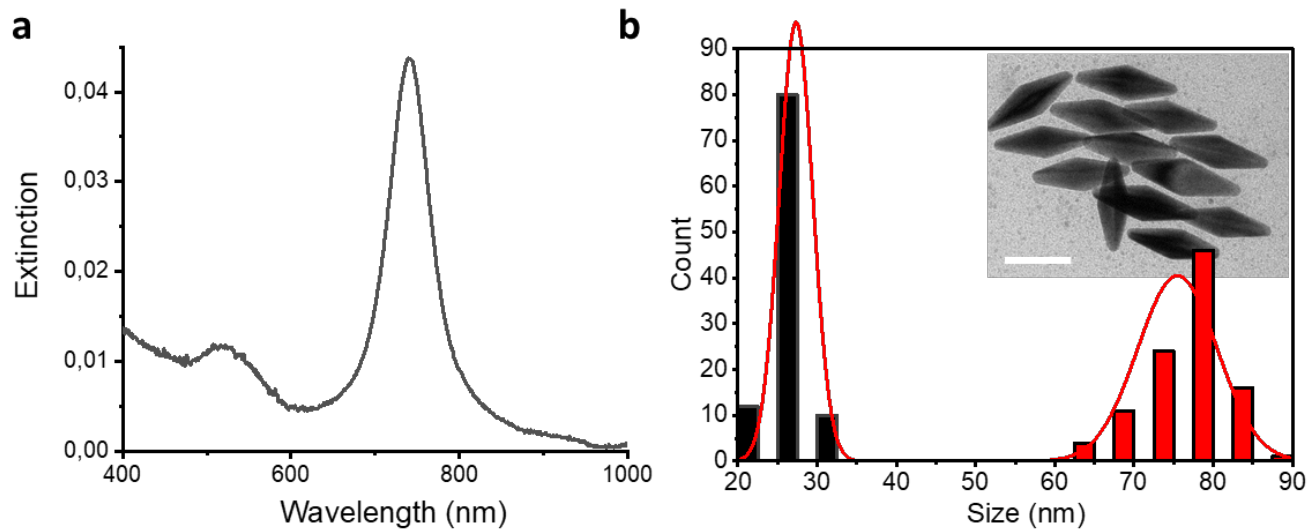


Figure S1: Characterization of the bipyramidal seed. **a)** UV-Vis spectra of the GBPs dispersion. **b)** Size histogram of the bipyramidal seed 75.5 ± 5.0 nm long (red); 27.3 ± 2.1 nm base-width (black) determined from TEM image analysis. Inset in b) shows a TEM image of the bipyramidal seeds.

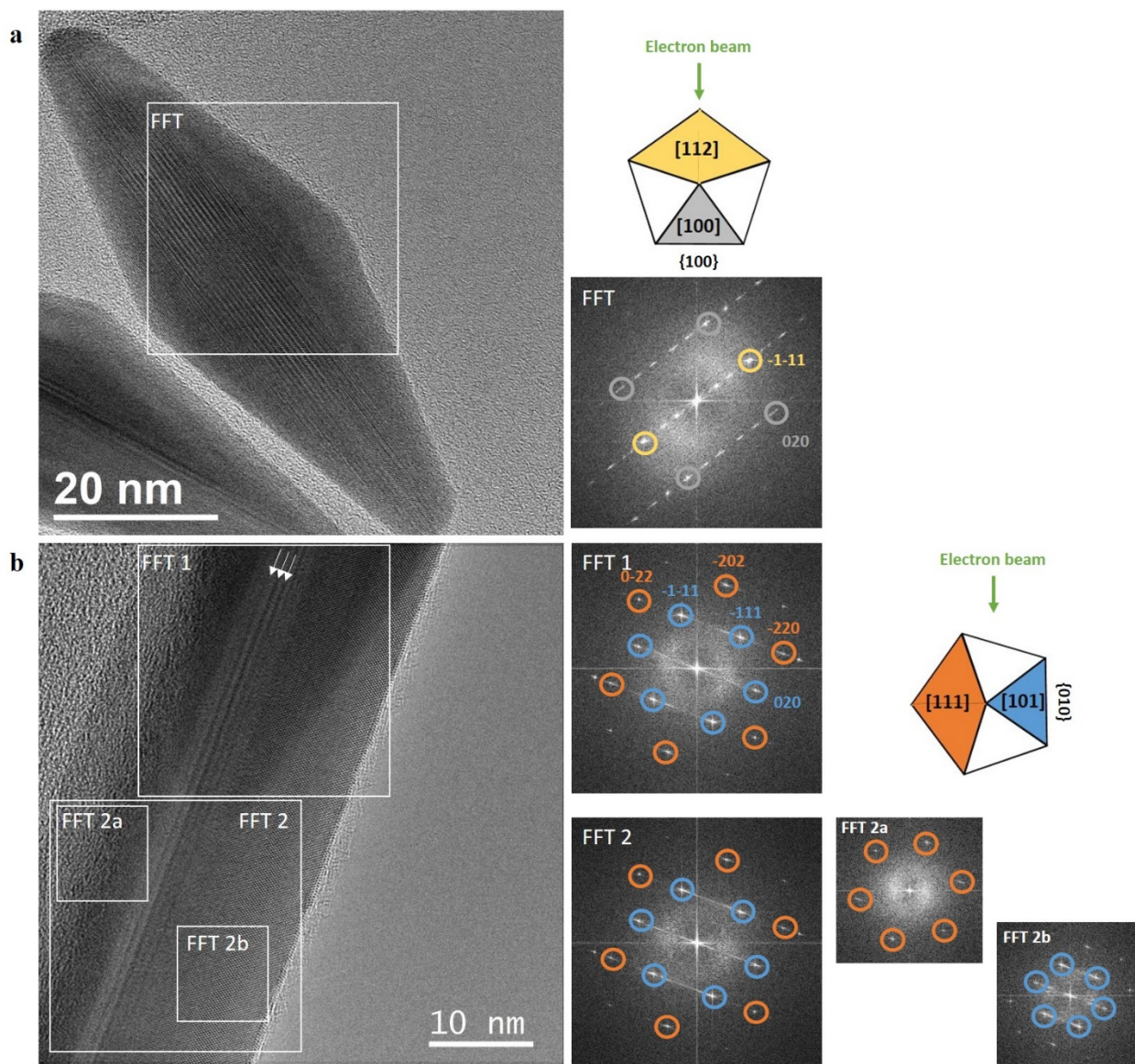


Figure S2. (a) HRTEM image of a bipyramidal seed. The Fast Fourier Transform (FFT) correspond to the superposition of two FCC crystals oriented along the $\langle 100 \rangle$ and $\langle 112 \rangle$ zone axes. As previously demonstrated,¹⁴ such atomic contrasts are characteristic of a penta-twinned nanostructure with one of its lateral $\{100\}$ facet (or edge for bipyramids) perpendicular to the electron beam (see scheme). (b) HRTEM image of an Au@Ag core-shell nanostructure. The FFT 1 and 2 show that the atomic structure of the rod is identical with (FFT 1) and without (FFT 2) the gold seed, suggesting the epitaxial growth of silver on the gold bipyramid. Note that gold and silver have the same FCC structure with similar lattice parameter (0.41 nm), favoring epitaxial relationship. The moiré pattern oriented along the anisotropy axis of the rod (white arrows) indicates its multiple-twinned structure, with twin planes that contain the anisotropy direction and propagate all along the rod. The FFT 1 and 2 correspond to the superposition of two FCC crystals oriented along the $\langle 111 \rangle$ and $\langle 101 \rangle$ zone axes. The FFT 2a and 2b show that the crystals oriented along the $\langle 111 \rangle$ and $\langle 101 \rangle$ zone axes are in the left and right parts of the rod, respectively. As

previously demonstrated,¹⁴ such atomic contrasts are characteristic of a penta-twinned nanorod with one of its lateral {010} facet parallel to the electron beam (see scheme).

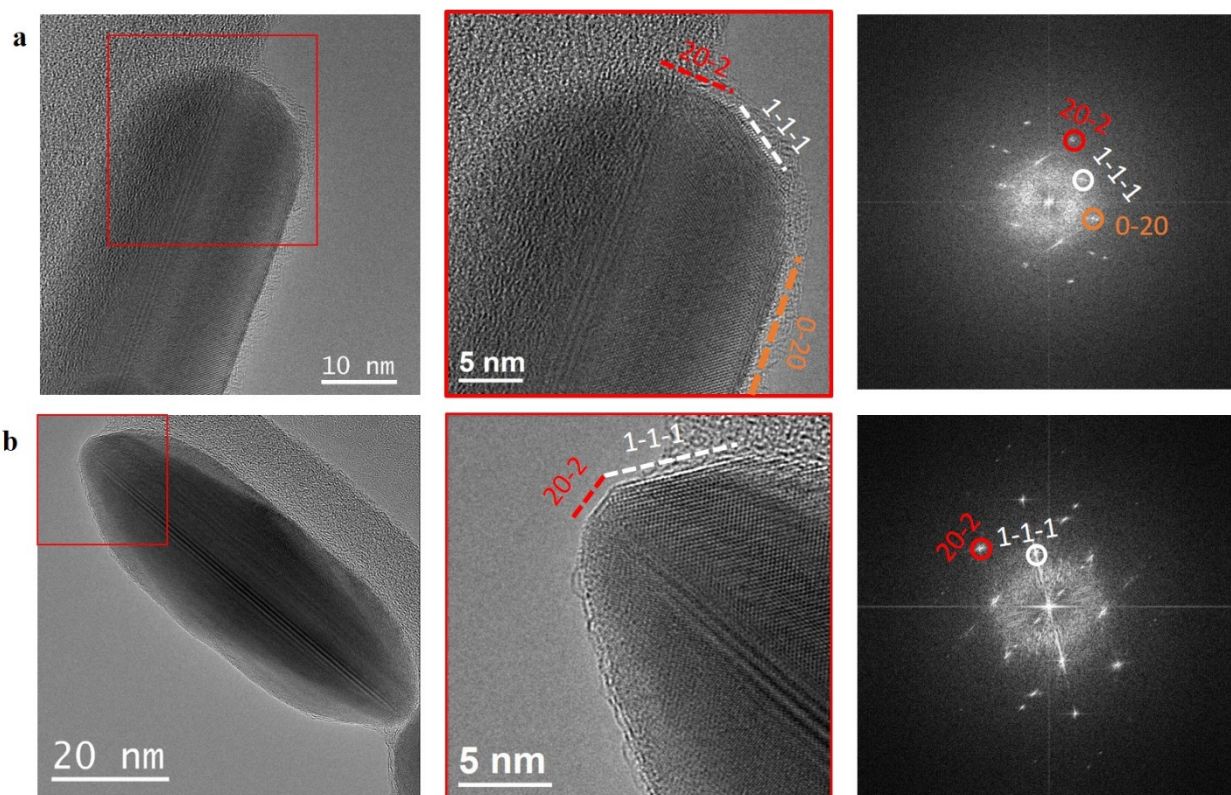


Figure S3. HRTEM imaging of the tip of (a) a long and (b) a short Au@Ag nanorod. The nanorod seen in (a) is the same as in figure S2b. The two penta-twinned nanorods have one of their lateral $\{010\}$ facets parallel to the electron beam. Along this orientation, one of the $\{111\}$ facets of the tip is clearly seen because it is also parallel to the electron beam (white dashed lines). The anisotropy axis of the rod is always the direction $\langle 110 \rangle$ and a short $\{110\}$ facet is observed at the apex of the rods (red dashed lines).

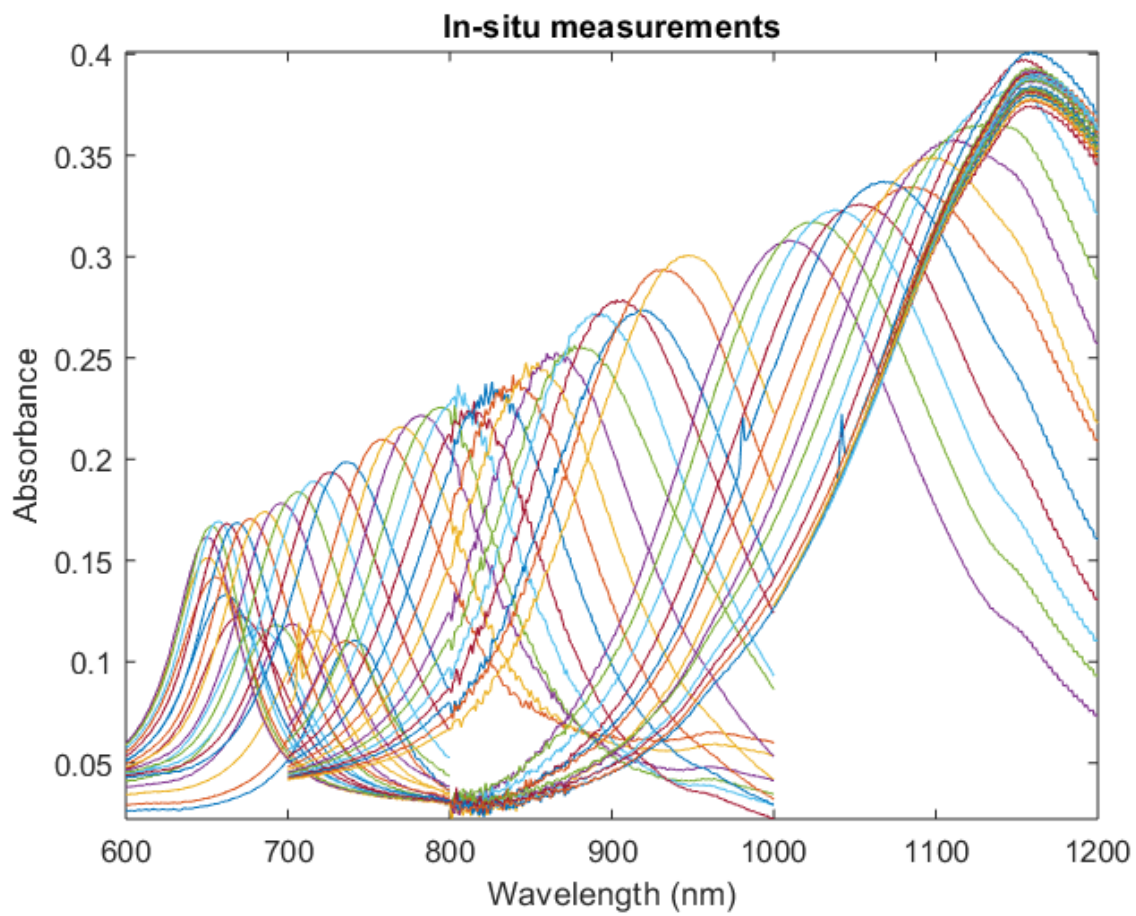


Figure S4. Series of *in situ* UV/Vis extinction spectra obtained at 60°C with an Ag/Au ratio of 3.

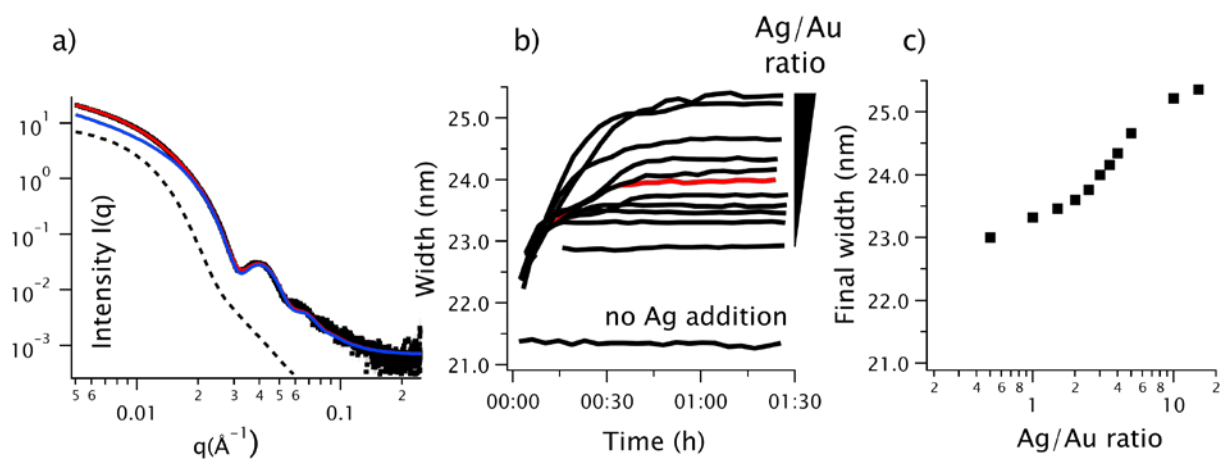


Figure S5. Particle width as extracted from the SAXS measurements. (a) Experimental intensity $I(q)$ from Figure 2b at time $t = 00:46:18$ (dots and error bars), with the complete fit (red line). The individual fit terms are also displayed: the polydisperse cylinder form factor (blue line) and the Beaucage model (black dashed line). (b) Width as a function of time for several Ag/Au ratios. The curve corresponding to the data in Figure 2b (Ag/Au = 3) is shown in red. (c) The final width as a function of the Ag/Au ratio.

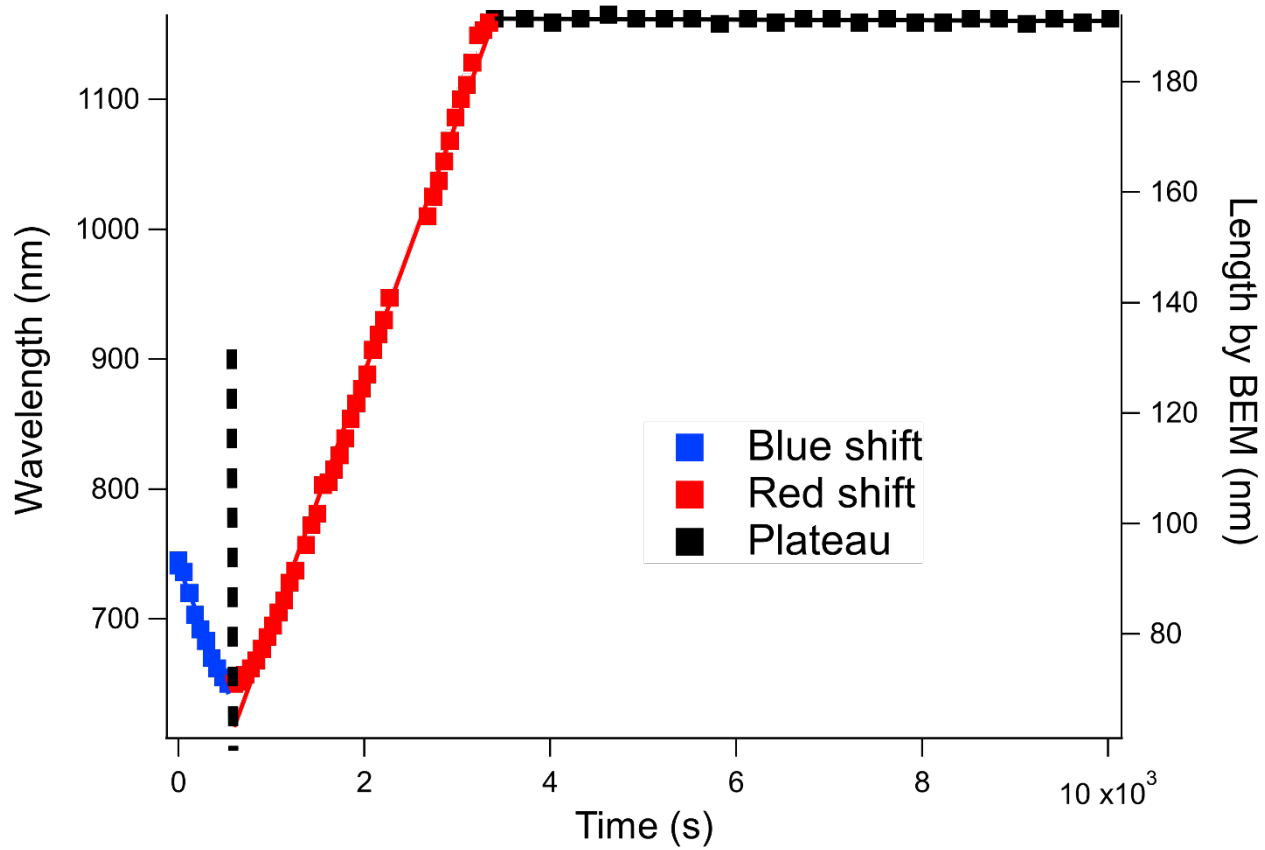


Figure S6. Position of the maximum of the longitudinal LSPR for the spectra in Supplementary Figure 4 as a function of time (left axis) and particle length extracted from the BEM simulations (right axis). The three different regimes (blue shift, red shift and stationary value) are highlighted by the symbol colors and fitted to linear variations (solid lines of corresponding color). The length calibration is only valid for time values above the dashed line (red shift and plateau regimes.)

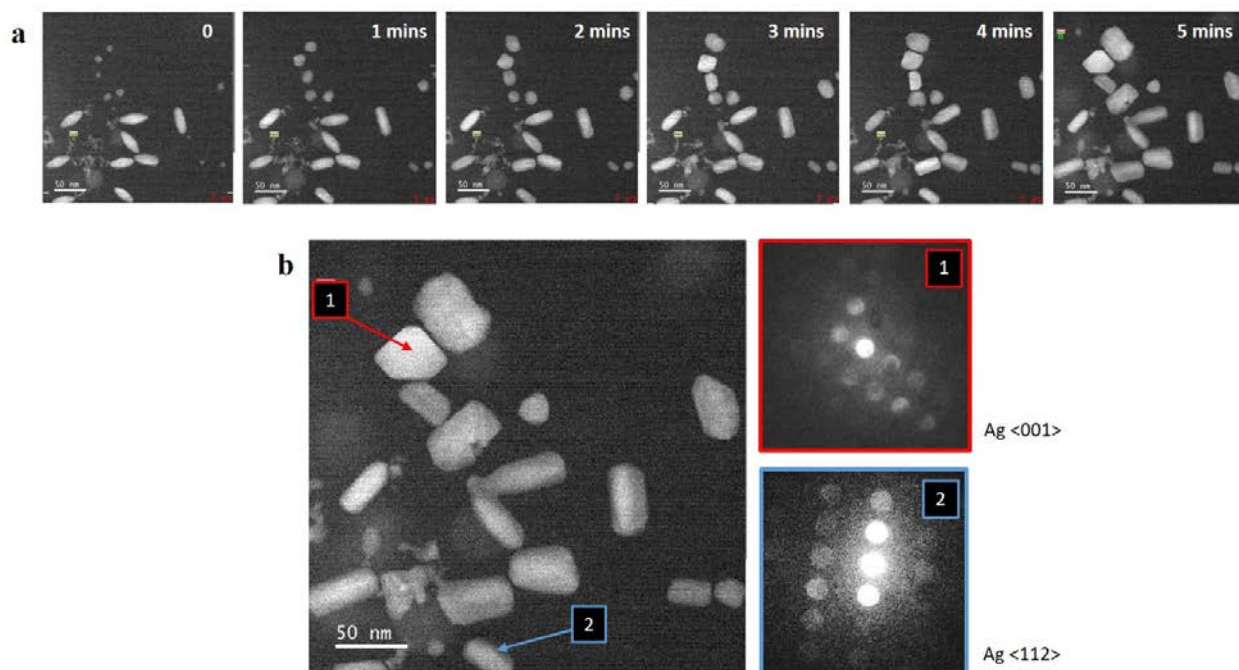


Figure S7. *In situ* structural analysis of Ag and Au@Ag nanoparticles. (a) Image series of a growth experiment performed without ascorbic acid. We observe the growth of faceted nanoparticles and isotropic shell on the gold bipyramids. (b) STEM nanodiffraction analyses performed after 5 minutes of growth on a faceted nanoparticle (diffraction 1) and on the shell of a bimetallic nanostructure (diffraction 2). The positions of the STEM nanoprobe (convergence angle of 7.4 mrad) are selected directly on the STEM HAADF image (left) and the diffractions of individual nano-objects (right) are acquired on a CCD camera. The diffractions 1 and 2 corresponds to the FCC structure of metallic silver oriented along the <001> and <112> directions, respectively. No other Ag crystalline phase was observed in the reaction media.

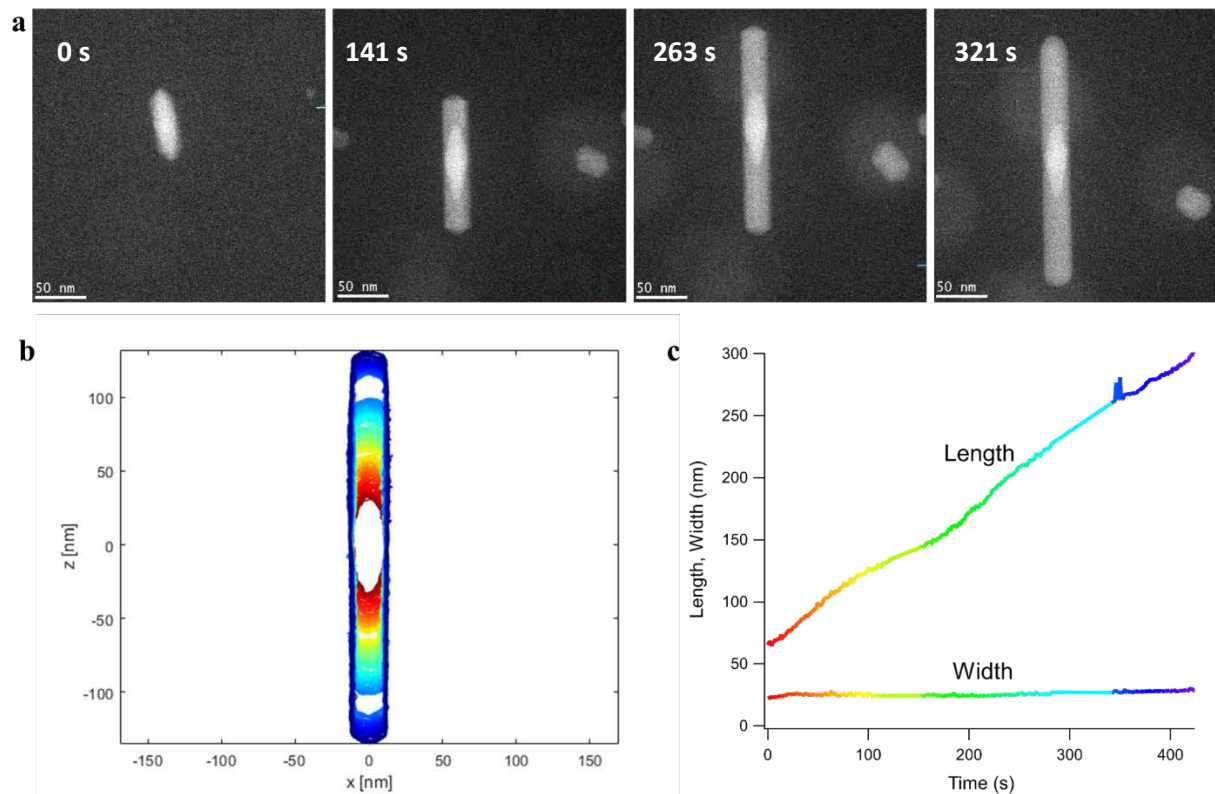


Figure S8. Long-term LCTEM growth experiment leading to the formation of a long (almost 300 nm) Au@Ag nanorod. (a) STEM HAADF image series. (b) Evolution of the nanorod contour plot over the experiment. (c) Length and width of the nanorod over time.

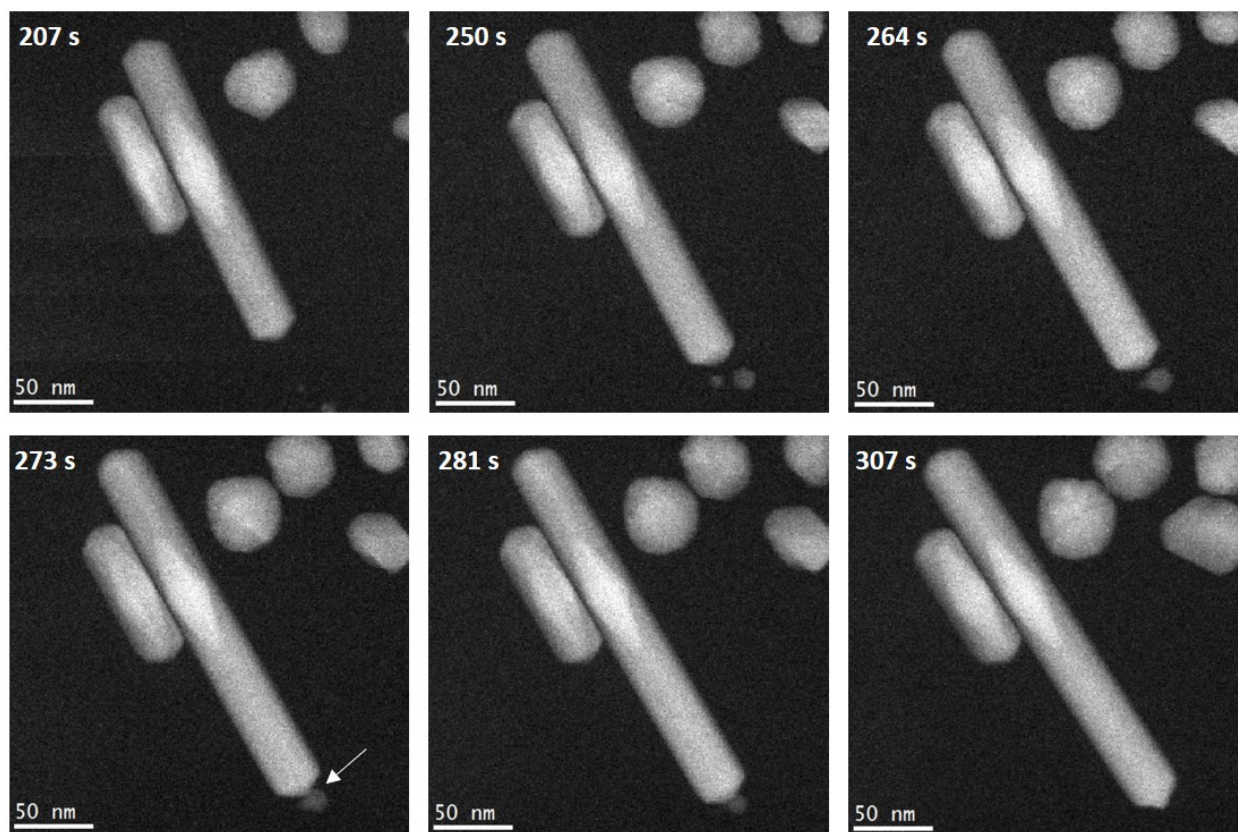


Figure S9. LCTEM image series showing a very rare coalescence event (white arrow) between a preformed Ag nanoparticles and a growing Au@Ag nanorod.

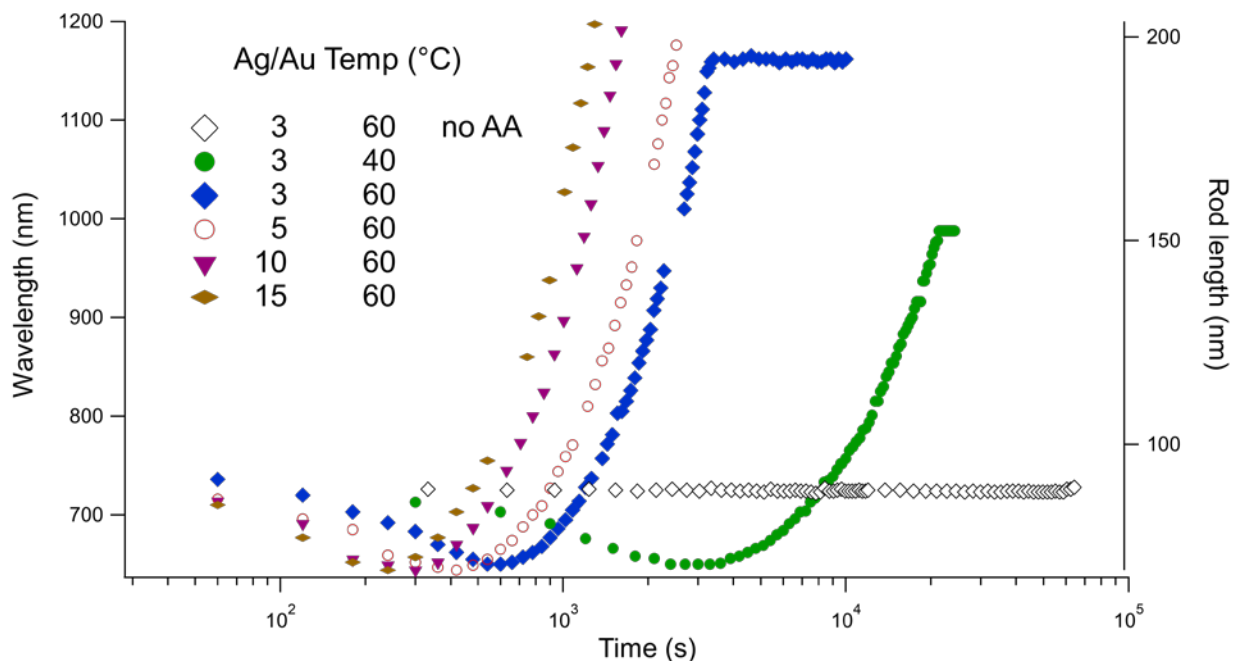


Figure S10. Investigation of the growth kinetics at other reaction temperatures and precursor concentrations

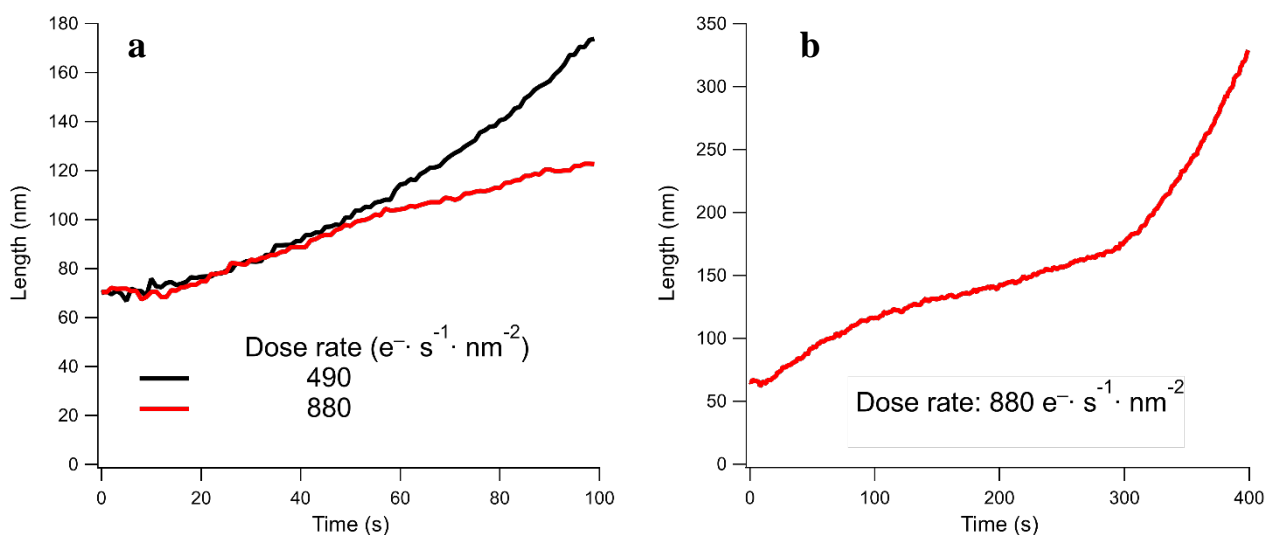


Figure S11. (a) Evolution of the nanorod length observed by LCTEM as a function of time for two different electron dose rates (i.e. different magnification). The graphs show that the average growth rate varies from 0.54 to 1.25 nm/s but it does not increase with the dose rate. It is worth noting that the growth of silver is only observed in the irradiated area, but the reaction kinetics is not controllable with the electron beam. (b) Evolution of the length of a nanorod as a function of time showing a strong acceleration of the growth rate although the electron beam illumination remains unchanged. The associated movie (accelerated 16 times) is available as Video_3.

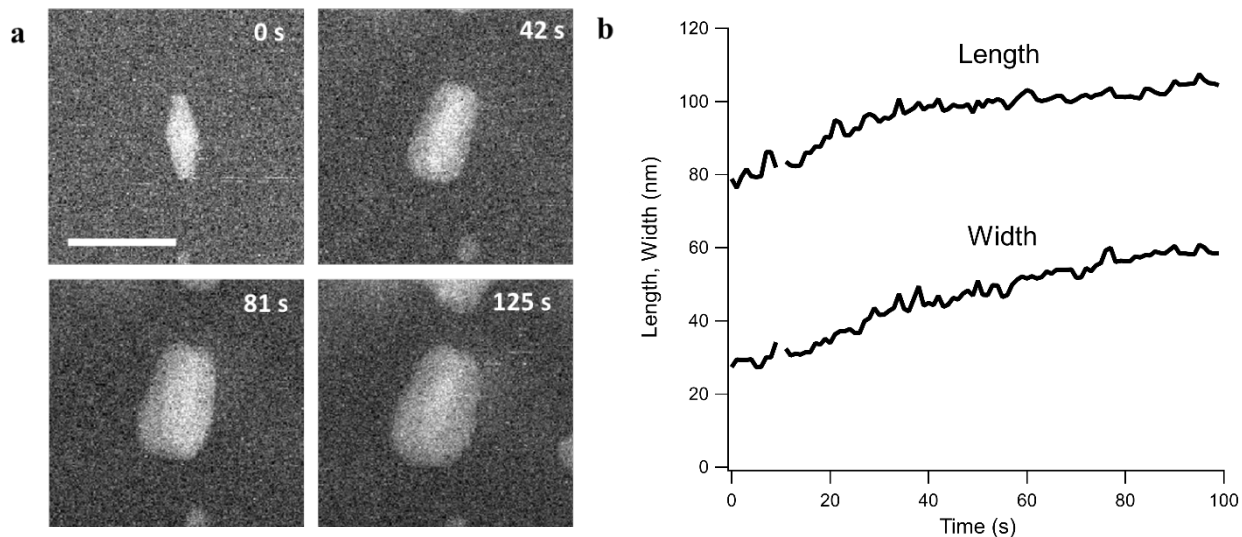


Figure S12. (a) Time series of STEM HAADF image showing the isotropic growth of silver on a gold bipyramid obtained without ascorbic acid. The scale bar corresponds to 50 nm. (b) Length and width of the nanostructure as a function of time.

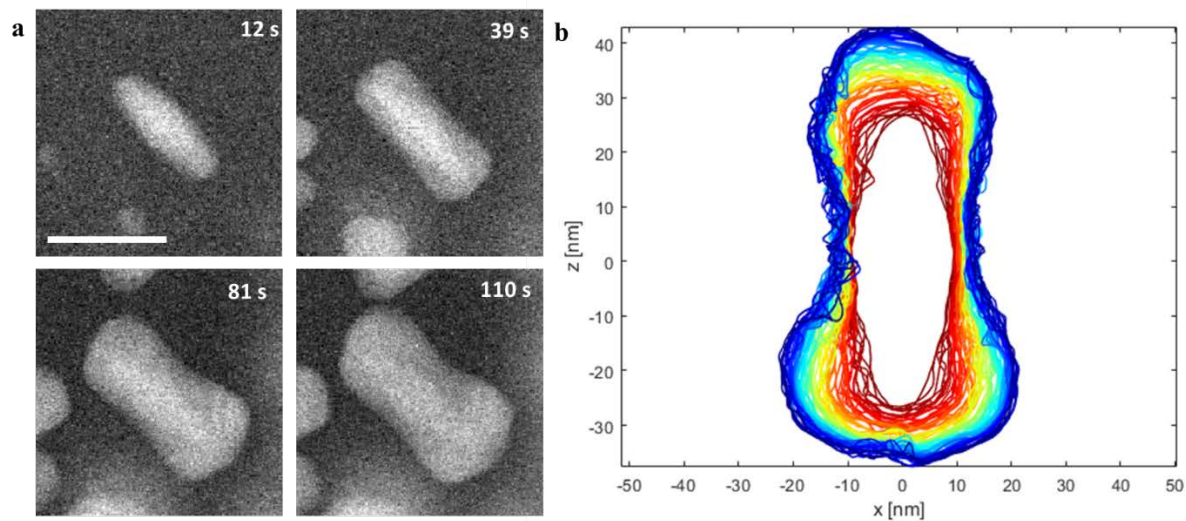


Figure S13. (a) Time series of STEM HAADF image showing the formation of a “dog-bone” Au@Ag nanostructure obtained without ascorbic acid. The scale bar corresponds to 50 nm. (b) Evolution of the nanorod contour plot over the experiment.

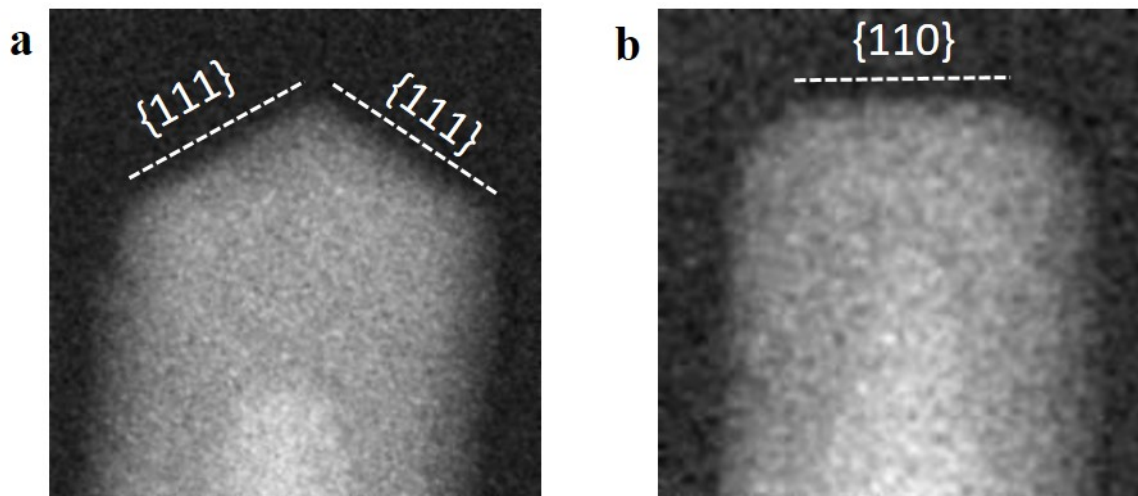


Figure S14. Image of the nanorod tip acquired during LCTEM growth experiments (a) with ascorbic acid and (b) without ascorbic acid. The indices of the tip facets inferred from these projected images of the nanostructures are specified.

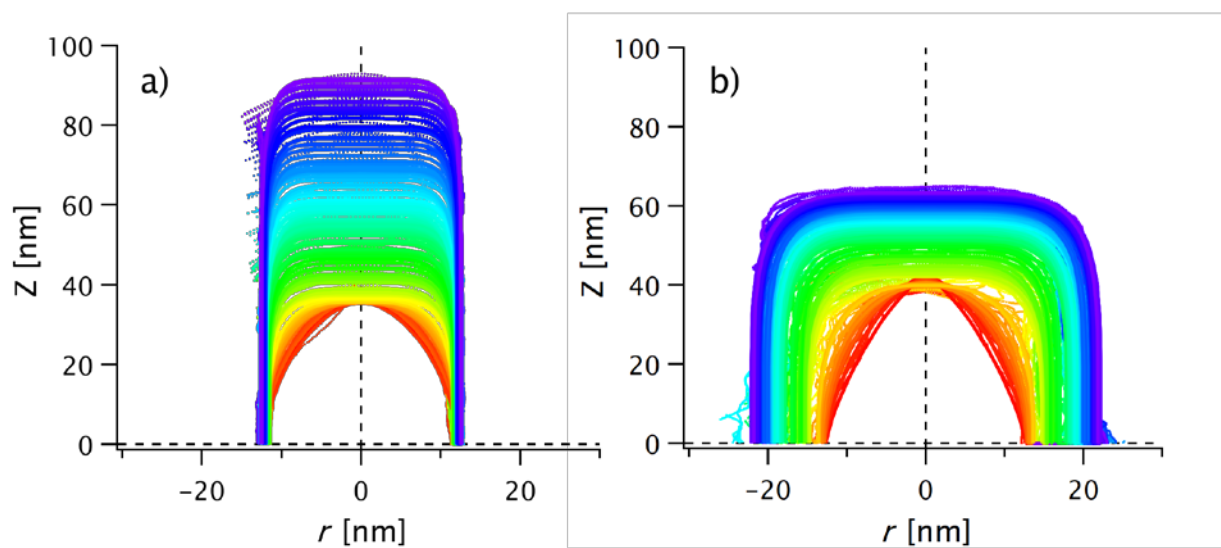


Figure S15. Comparison between the experimental outlines (dots) and the fits (solid lines). a) with ascorbic acid (Figs 3b and 3c) and b) without ascorbic acid (Fig 4b and corresponding fits).

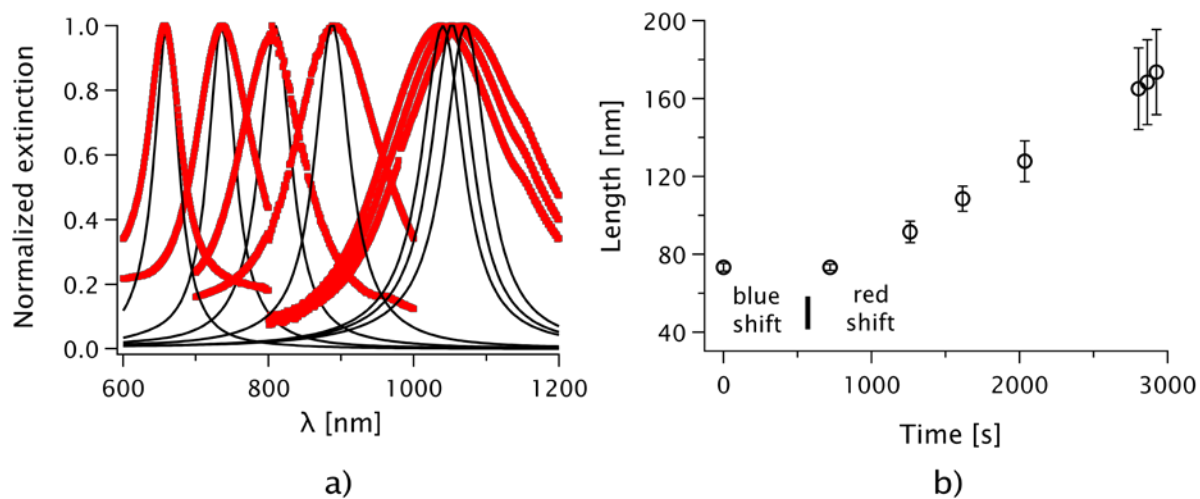


Figure S16. a) Some of the data in Figure S4 (red dots) and BEM simulations for Au@Ag nanorods yielding the same peak position. b) Average particle length (symbols) and polydispersity (error bars) for the curves in a), as a function of time. The values for the seeds (gold bipyramids) are shown for $t = 0$ s.

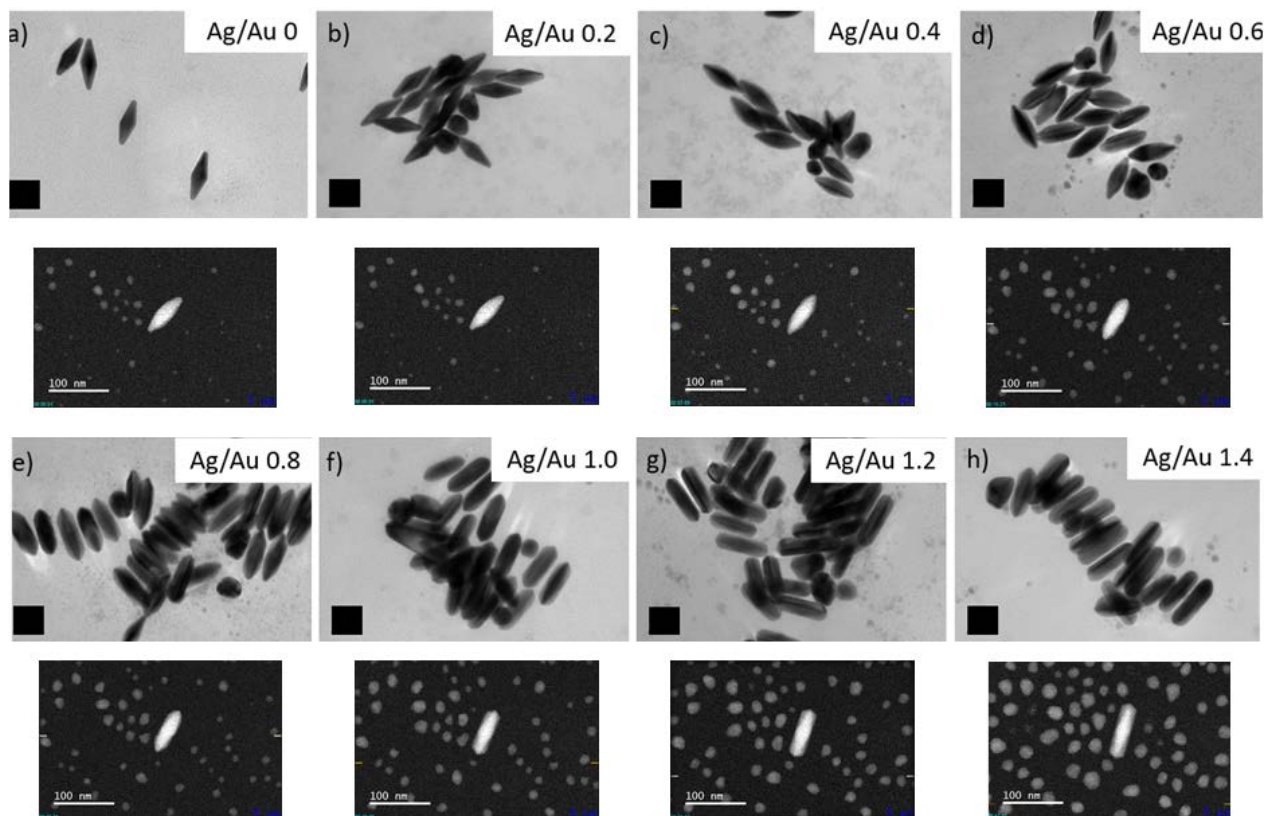


Figure S17. a) to e), top row: TEM images for the final state of the synthesis at various Ag/Au ratios (indicated on the images). The scale bar (black box) is 50 nm. Bottom row: LC-TEM images selected from the kinetics presented in Figure 3 of the main text (also Video_1.) The scale bar (thin white line) is 100 nm; the scale is the same in the TEM and LC-TEM images.

Supplementary Movies

Video files available with this submission:

1. The full kinetics corresponding to the images in Fig. 3a, accelerated 16 times (Video_1).
The real time stamp can be seen in the bottom left corner.
2. The full kinetics corresponding to the images in Fig. 4a, accelerated 16 times (Video_2).
The real time stamp can be seen in the bottom left corner.
3. The full kinetics corresponding to the data in Fig. S11b, accelerated 16 times (Video_3).
The real time stamp can be seen in the bottom left corner.

References

1. Chateau, D.; Liotta, A.; Vadcard, F.; Navarro, J. R.; Chaput, F.; Lerme, J.; Lerouge, F.; Parola, S. From gold nanobipyramids to nanojavelins for a precise tuning of the plasmon resonance to the infrared wavelengths: experimental and theoretical aspects. *Nanoscale* 2015, 7 (5), 1934-43.
2. Sanchez-Iglesias, A.; Winckelmans, N.; Altantzis, T.; Bals, S.; Grzelczak, M.; Liz-Marzan, L. M. High-Yield Seeded Growth of Monodisperse Pentatwinned Gold Nanoparticles through Thermally Induced Seed Twinning. *J. Am. Chem. Soc.* 2017, 139 (1), 107-110.
3. Park, K.; Drummy, L. F.; Vaia, R. A. Ag shell morphology on Au nanorod core: role of Ag precursor complex. *J. Mater. Chem.* 2011, 21 (39), 15608-15618.
4. Hamon, C.; Goldmann, C.; Constantin, D. Controlling the symmetry of supercrystals formed by plasmonic core-shell nanorods with tunable cross-section. *Nanoscale* 2018, 10 (38), 18362-18369.
5. Tebbe, M.; Kuttner, C.; Mayer, M.; Maennel, M.; Pazos-Perez, N.; König, T. A. F.; Fery, A. Silver-Overgrowth-Induced Changes in Intrinsic Optical Properties of Gold Nanorods: From Noninvasive Monitoring of Growth Kinetics to Tailoring Internal Mirror Charges. *J. Phys. Chem. C* 2015, 119 (17), 9513-9523.
6. Alloyeau, D.; Dachraoui, W.; Javed, Y.; Belkahla, H.; Wang, G.; Lecoq, H.; Ammar, S.; Ersen, O.; Wisnet, A.; Gazeau, F.; Ricolleau, C. Unravelling Kinetic and Thermodynamic Effects on the Growth of Gold Nanoplates by Liquid Transmission Electron Microscopy. *Nano Lett.* 2015, 15 (4), 2574-2581.
7. Piffoux, M.; Ahmad, N.; Nelayah, J.; Wilhelm, C.; Silva, A.; Gazeau, F.; Alloyeau, D. Monitoring the dynamics of cell-derived extracellular vesicles at the nanoscale by liquid-cell transmission electron microscopy. *Nanoscale* 2018, 10 (3), 1234-1244.
8. Khelfa, A.; Byun, C.; Nelayah, J.; Wang, G.; Ricolleau, C.; Alloyeau, D. Structural analysis of single nanoparticles in liquid by low-dose STEM nanodiffraction. *Micron* 2019, 116, 30-35.
9. Hohenester, U.; Trügler, A. MNPBEM – A Matlab toolbox for the simulation of plasmonic nanoparticles. *Comput. Phys. Commun.* 2012, 183 (2), 370-381.
10. Johnson, P. B.; Christy, R. W. Optical Constants of the Noble Metals. *Phys. Rev. B* 1972, 6 (12), 4370-4379.
11. Kline, S. Reduction and analysis of SANS and USANS data using IGOR Pro. *J. Appl. Crystallogr.* 2006, 39 (6), 895-900.
12. Thomas, N.; Mani, E. An analytical solution to the kinetics of growth of gold nanorods. *RSC Advances* 2016, 6 (36), 30028-30036.

13. Avrami, M. Kinetics of Phase Change. II Transformation-Time Relations for Random Distribution of Nuclei. *J. Chem. Phys.* 1940, 8 (2), 212-224.

14. Johnson, C. J.; Dujardin, E.; Davis, S. A.; Murphy, C. J.; Mann, S. Growth and form of gold nanorods prepared by seed-mediated, surfactant-directed synthesis. *J. Mater. Chem.* 2002, 12 (6), 1765-1770.